Ground Support 2026 - D Cumming-Potvin & J Wesseloo (eds.)
© 2026 Australian Centre for Geomechanics, Perth
doi:10.36487/ACG_repo/2625_27

# An unsupervised manifold learning framework for automated identification of rock discontinuities in underground mines using raw LiDAR point cloud

**Zhen Han [a], Adam Schwartzkopff [b], Tony Joseph Mathew [c], Moe Moridi [d], Selahattin Akdag [a,*]**

[a] *Western Australian School of Mines, Curtin University, Australia*

[b] *Department of Civil, Environmental and Mining Engineering, The University of Western Australia, Australia*

[c] *Centre for Optimisation and Decision Science, Curtin University, Australia*

[d] *Evolution, Australia*

## Abstract

*Accurate mapping of rock discontinuities is essential for rock mass characterisation, stability analysis and ground-support design. Traditional manual approaches are time-consuming, labour-intensive, and subjective in interpretation. Digital approaches based on photogrammetry and Light Detection and Ranging (LiDAR) point cloud methods provide efficient tools for solving the problem. However, photogrammetry-based methods are challenging due to the low-light and dusty underground environments, making LiDAR point cloud data a superior tool to the traditional approach, which can actively emit lasers and is therefore independent to the illumination conditions. Supervised deep learning-based methods are widely adopted for 3D point cloud analysis in underground constructions due to their robust performance. Although the performance of these models is enhanced by adopting advanced deep learning strategies, the application and generalisation ability of these methods are limited by the supervised manner, which requires extensive labelled datasets. Therefore, this study proposes a novel unsupervised deep neural network-based method (ManiRock) for automatic rock discontinuities identification from LiDAR point clouds. We integrate a state-of-the-art unsupervised implicit learning method and a widely used clustering method. ManiRock directly takes the raw point cloud as input and constructs a continuous implicit representation of the rock surface manifold and identify and isolate each discontinuity subsequently in a two-step manner. This study provides a case study as a geometric proof-of-concept using limited unsupported underground tunnel rock mass point clouds. The method is tested using LiDAR point cloud datasets acquired from a metal mine located in Kalgoorlie, Western Australia. The results are compared with ground-truth results derived from manual mapping and demonstrate that ManiRock achieves high-fidelity discontinuity mapping while bypassing the need for data labelling, providing a potentially useful tool for rapid geotechnical assessment of underground rock mass.*

***Keywords:*** *rock mass discontinuities, LiDAR, unsupervised manifold learning*

## 1 Introduction

Rock masses consist of the intact rocks together with discontinuities (Palmström 1996). The spatial characteristics of the discontinuities, which generally include orientation, trace length, spacing, aperture, and roughness, are crucial in governing the stability and mechanical properties of rock masses (Kinde et al. 2024; Priest 1993; Pu et al. 2025; Zhan et al. 2017a). Accurate characterisation of discontinuities in underground tunnels is essential in selecting optimised excavation methods, designing tunnel support systems, and ensuring the safety of underground construction (Assali et al. 2016; Boon et al. 2014; Maria et al. 2004).

[*] Corresponding author. Email address: sela.akdag@curtin.edu.au

Traditionally, manual contact-based methods are adopted for retrieving these parameters by using geological compass, clinometer, and measuring tape (Assali et al. 2016; Chen et al. 2021; Erharter et al. 2024; Fecker & Rengers 1971; Gomes et al. 2016; Lato & Vöge 2012; Milne et al. 1998). Contact-based methods are inherently time-consuming and labour-intensive. These methods also require field work in potentially dangerous environments (Fecker & Rengers 1971), the datasets are discrete (Chen et al. 2021) and the interpretations of the results are highly subjective (Ferrero et al. 2014; Zhan et al. 2017b).

The development of remote sensing-based digital methods has enabled non-contact methods for rock mass characterisation, which mainly includes photogrammetry and Light Detection and Ranging (LiDAR) technologies (Chen et al. 2023). However, the photogrammetry-based methods require high-quality images captured under optimal illumination conditions, which greatly hinders it from being applied to underground environments (Xu & Tang 2025). On the contrary, LiDAR directly collects 3D coordinates, known as a point cloud, of the targets in an active manner without requiring environment illumination, making LiDAR a superior option for collecting rock mass information in complex low-light underground tunnels (Han et al. 2025; Han et al. 2026). Many developments have been made on rock mass characterisation using LiDAR point cloud. The key step is to identify the discontinuities of the rock masses. These methods can be divided into classical geometric and rule-based methods, traditional machine learning methods, and deep learning methods. Region growing and voxel-based algorithms are commonly adopted algorithms of the first type (Battulwar et al. 2021; Gigli & Casagli 2011; Yi et al. 2023). These methods require extensive manually designed rules, which is more suitable for regular shape recognition. Clustering is a dominant traditional machine learning method for rock discontinuity identification (Li et al. 2025a; Singh et al. 2021; Tang et al. 2023; Wang et al. 2026; Zhou et al. 2024). Deep learning methods utilise more complex deep neural networks and can achieve end-to-end discontinuity identification without manual feature engineering (Battulwar et al. 2024; Ge et al. 2025; Li et al. 2023; Zhou et al. 2025). The classical geometric and rule-based methods require extensive manually designed rules and are more suitable for detecting regular shapes. The traditional machine learning methods, especially the clustering-based methods are widely adopted due to their simplicity but stronger adaptability to various rock mass geometries. Deep learning methods show the most powerful ability for fitting non-linear relationships; however, they require enormous data collection and labelling processes, which is challenging especially for underground mine tunnels. Therefore, this research aims to provide a balanced hybrid method for identifying rock mass discontinuities that keeps both efficiency of the clustering-based methods and accuracy of deep learning but in an unsupervised manner.

Normal vectors are a key feature representing point cloud geometry and a key for clustering-based discontinuity identification methods. Clustering-based methods can generate groups of planar surfaces based on the distribution of normals. Based on the classified clusters, each surface can be easily isolated. However, traditionally, the normal vectors are derived from the principal component analysis (PCA), which generates the normal vectors using local fitting. PCA heavily relies on the selected scale for fitting the planar surface. In the drill-and-blast underground tunnels, the rock surfaces are extremely rough and contain sharp changes, which can lead to great errors when the scale is mismatched. Deep learning methods have provided powerful approaches for correctly estimating normals (Li et al. 2022, 2024), however, they require a large amount of training data pairs. On the contrary, unsupervised neural implicit learning represents a new trend for reconstructing 3D geometries from raw point cloud and can output a consistent normal field by learning a valid manifold from the raw point cloud data without requiring data labelling process. This research uses an unsupervised implicit learning method to rebuild the manifold of the rock mass surface to derive the normal field and identify the discontinuities based on clustering. As the core of the method relies on the manifold construction of rock mass surface point cloud, we call this method ManiRock. Rock mass point cloud data are collected in an underground mine and in the experiment the overall average precision, accuracy and F1 score, (which is a harmonic mean of precision and recall) of ManiRock are 0.937, 0.875, and 0.900, respectively.

# 2 Data collection and preprocessing

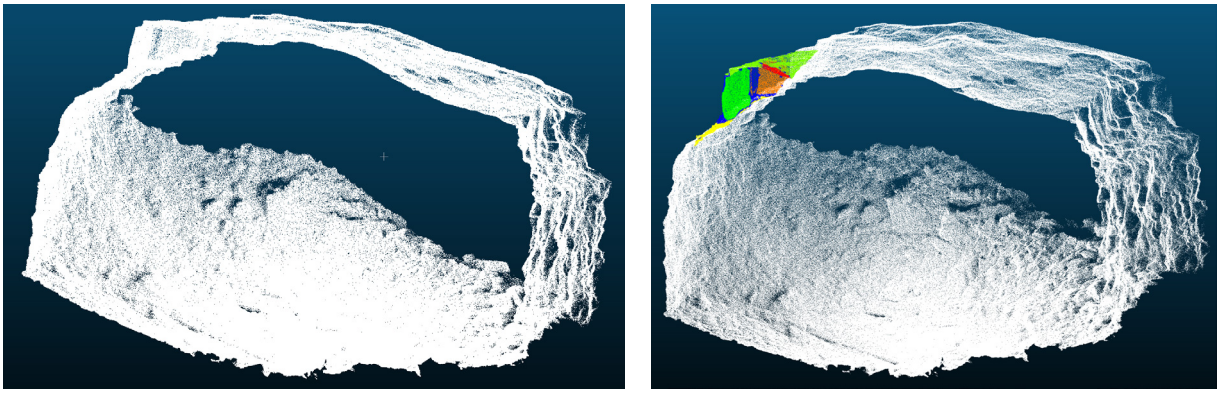
The rock mass point cloud data were collected using a hand-held Hovermap ST LiDAR, which is a simultaneous localization and mapping (SLAM) LiDAR, from an underground metal mine located in Kalgoorlie, Western

Australia. A tunnel section approximately 5 m high, 10 m wide, and 4 m along the tunnel axis, containing 4,131,640 points was used to optimise the implicit model. Table 1 lists the specifications of the LiDAR system.

**Table 1 Specifications of the LiDAR system**

| Parameters | Descriptions |
|---|---|
| Laser scanner | Hovermap ST AUTONOMY |
| SLAM mapping | SLAM based LiDAR mapping ± 0.03% drift |
| Field of view | 360 × 290° |
| LiDAR range | 0.40–100 m |
| LiDAR accuracy | ± 30 mm |
| Mapping accuracy | ± 15 mm (19/32 in) in typical underground and indoor environments |
| Point cloud attributes | Intensity, range, time, return number (strongest and last) and ring number |
| Data acquisition speed | Single Return Mode: up to 300,000 points/s<br>Dual Return Mode: up to 600,000 points/s |

Figure 1a shows the section of the underground metal mine tunnel point cloud and Figure 1b shows the selected part for the validation, which is visualised in colours.



(a) (b)

**Figure 1 Dataset. (a) A section of the underground metal mine tunnel point cloud; (b) A part of the unsupported area, shown in colours with each colour representing a manually identified discontinuity, is used for the validation work. It should be noted that from a practical ground-support design perspective, the focus is usually on the main structural sets rather than mapping several individual discontinuity patches within such a small area and this case study adopts a geometric, instance-level segmentation test for validation**

# 3 Methodology

The proposed framework provides a hybrid method integrating an unsupervised neural implicit learning to derive the normal field and a density-based clustering method (DBSCAN) (Ester et al. 1996) to retrieve single discontinuity surfaces, shown in Figure 2. The rock mass point cloud was represented by a neural implicit function by training an artificial neural network in an unsupervised manner. Then, the normal fields were derived from the neural network and used for clustering. The individual discontinuities were isolated based on connected component analysis. DBSCAN first was applied based on the rock mass surface point cloud normal orientation feature space and then applied again based on the 3D Euclidean space on the rock mass point cloud to isolate each single entity. The top 5 discontinuities were selected according to the total number of points each identified discontinuity contains. Finally, precision, recall and F1 score (defined in Section 3.3)

were calculated compared to the manually identified discontinuities to comprehensively evaluate the performance of ManiRock.

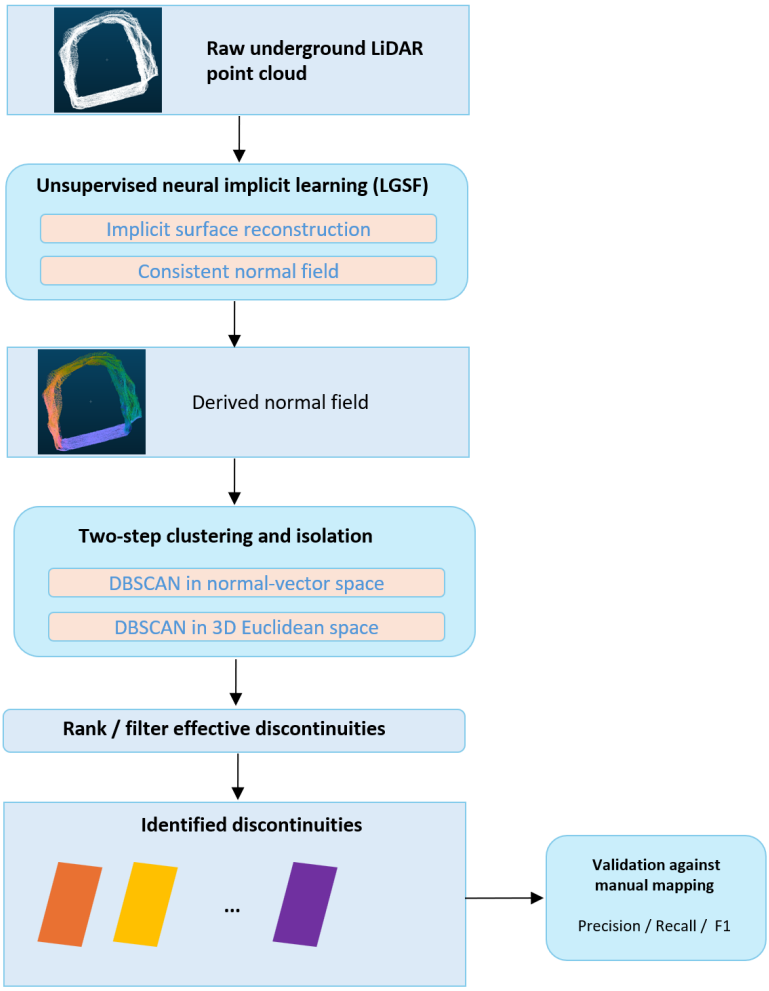



**Figure 2 ManiRock architecture**

## 3.1 Constructing the rock mass surface point cloud manifold

Normal orientation and distribution of rock mass surface point cloud is a key feature for identifying discontinuities. To derive a more consistent and accurate global normal field from the raw point cloud, the unsupervised neural implicit learning method based on the local gradient-aware surface filtering (LGSF) architecture (Li et al. 2025b) was adopted to construct the valid manifold representing the rock mass surface geometry. Let $\mathcal{P} = \{\mathbf{p}_i\}_{i=1}^{N} \subset \mathbb{R}^3$ denote the raw point cloud, which inherently contains high-frequency noise induced by drill-and-blast excavation. $\mathbf{p}_i$ means the $i-th$ point and N is the total number of points in the raw point cloud. The objective is then to learn a continuous signed distance function $f_\theta: \mathbb{R}^3 \to \mathbb{R}$, where its zero-level set represents the underlying rock surface. $\theta$ in $f_\theta$ represents learnable parameters.

### *3.1.1 Spatial projection and implicit field initialisation*

To enable the model to gain a spatial sense of the surrounding of the tunnel surface, an auxiliary query point set $\mathcal{Q} = \{\mathbf{q}_i\}_{i=1}^{N}$ was constructed by adding adaptive Gaussian noise to $\mathcal{P}$. $\mathbf{q}_i$ is the $i-th$ point in the auxiliary query point set. The query points were projected onto the zero-level set by utilising the network's predicted signed distance $f_\theta(q_i)$ and the analytical spatial gradient to form the surface point set $\mathcal{Q}'$:

$$\mathbf{q}_i' = \mathbf{q}_i - f_\theta(\mathbf{q}_i) \cdot \mathbf{n}_{\mathbf{q}_i} \quad (1)$$

where

$\mathbf{q}_i'$ = the $i-th$ point in the surface point set

$\mathbf{n}_{\mathbf{q}_i} = \frac{\nabla f_\theta(\mathbf{q}_i)}{\|\nabla f_\theta(\mathbf{q}_i)\|}$ = the gradient direction at the query point.

### *3.1.2 Geometric surface fitting*

To prevent the learned implicit surface from over-fitting to local anomalies (e.g. small craters caused by blasts), a robust three-way distance measurement operator was adopted as a loss function for restricting the neural network to learn the surface geometry as follows:

$$\mathcal{L}_d = \frac{1}{N}\sum_{i=1}^{N}(\|\mathbf{q}_i' - \mathbf{p}_i\| + |(\mathbf{q}_i' - \mathbf{p}_i)\mathbf{n}_{\mathbf{p}_i}^{\top}| + |(\mathbf{q}_i' - \mathbf{p}_i)\mathbf{n}_{\mathbf{q}_i'}^{\top}|) \quad (2)$$

This operator comprehensively minimises the Euclidean distance errors from multiple perspectives. It considers both the direct point-to-point distance and the projection distances along the raw noise normal $\mathbf{n}_{\mathbf{p}_i}$ and the surface normal $\mathbf{n}_{\mathbf{q}_1'}$.

A signed distance loss function was simultaneously applied to restrict the zero-set level to approach the underlying rock mass point cloud surface by enforcing the surface points $\mathbf{q}_i'$ to approach the zero-level set:

$$\mathcal{L}_{sd} = \frac{1}{N}\sum_{i=1}^{N}(|f_\theta(\mathbf{q}_i')|^2 + |f_\theta(\mathbf{q}_i)|^2 + |f_\theta(\mathbf{p}_i)|^2) \quad (3)$$

### *3.1.3 Multi-scale gradient regularisation*

To overcome gradient degradation caused by severe geometric discontinuities in rock masses, 2 gradient consistency mechanisms were adopted to regularise the implicit field. The gradients between neighbouring level sets (i.e. not only the zero-level set was considered) were aligned using a confidence-weighted penalty with hyper parameter $\rho$ to control the decay rate, ensuring topological stability:

$$\mathcal{L}_n = \frac{1}{N}\sum_{i=1}^{N}(1 - \mathbf{n}_{\mathbf{q}_i}\mathbf{n}_{\mathbf{q}_i}^{\top}) \cdot \exp(-\rho \cdot |f_\theta(\mathbf{q}_i)|) \quad (4)$$

To achieve consistent structural orientations across varying rough scales, an additive normal $\bar{n}_{q_i} = \frac{\mathbf{n}_{\mathbf{q}_i} + \mathbf{n}_{\mathbf{q}_i'}}{\|\mathbf{n}_{\mathbf{q}_i} + \mathbf{n}_{\mathbf{q}_i}\|}$ was introduced. The averaged normal is optimised to align with the multi-scale geometric vectors $H_j(q_i)$ extracted from $N_K$ different neighbourhood scales with each $H_j(q_i)$ representing the oriented vector from the geometric centre of the $j$-th neighbourhood to the query point $q_i$:

$$L_v = \sum_{j=1}^{N_K}\frac{1}{N}\sum_{i=1}^{N}\| f_\theta(q_i) \cdot \bar{n}_{q_i} - H_j(q_i)\| \quad (5)$$

### *3.1.4 Optimisation and structural normal extraction*

The following total loss was used to optimise the neural implicit function through the backpropagation in a skip-connected multi-layer perceptron:

$$\mathcal{L} = \mathcal{L}_{sd} + \mathcal{L}_v + \lambda_1\mathcal{L}_d + \lambda_2\mathcal{L}_n \quad (6)$$

where $\lambda_1$ and $\lambda_2$ are weighting coefficients.

After convergence, for any raw rock mass point $\mathbf{p} \in \mathcal{P}$, its final normal $\mathbf{n}_\mathbf{p}$ was directly derived from the trained neural network. A neighbourhood aggregation strategy was adopted instead of directly using the single prediction at the point:

$$n_p = \frac{1}{\kappa+1}(\bar{n}_p + \sum_{i=1}^{\kappa}\bar{n}_i' \cdot \mu_i) \quad (7)$$

Where the weight $\mu_i = exp(-\delta_i - \phi(\bar{n}_i', \bar{n}_p))$ intelligently suppresses neighbouring points with low spatial proximity based on their spatial proximity $\delta_i$ and normal similarity $\phi$. This strategy ensures the derived

normals are highly resilient to localised blasting artifacts, generating a more robust normal field required by the following clustering steps.

#### *3.1.5 Implementation*

The core architecture was constructed based on a local patch feature extractor followed by a series of Multi-layer Perceptrons with a skip connection to approach the implicit surface geometry. Specifically, the network first maps coordinates of an input point patch of the rock mass into a higher-dimensional latent space through a shared multi-layer encoder with progressive channel dimensions of (64, 128, 256, 512). Each fully connected layer in the encoder is followed by a 1 D Batch Normalisation and a ReLU non-linear activation function to capture robust geometric representations of the point cloud. Adam optimiser was used to optimise the network parameters. Same learning strategies and loss weights were used as proposed in LGSF work (Li et al. 2025b). The experiments were conducted under a Linux operating system on a desktop with an Intel Core i9 14900K CPU, NVIDIA RTX4080 Super GPU and the computing takes around 155 s for deriving the normal field.

### 3.2 Clustering and isolation

The normal of each point was attributed to the original raw point cloud of the tunnel section. An unsupported section on the tunnel surface with clear structural differences was selected for test and validation. To automatically extract individual discontinuities from the unorganised point cloud, a two-step clustering approach based on DBSCAN was proposed. This approach operates progressively in both the normal vector feature space and the 3D Euclidean space.

Let the point cloud subset used for the clustering process be defined as $P_{sub} = \{p_1, p_2, \dots, p_M\}$, where $P_{sub} \subset P$ ($P$ denotes the raw point cloud of the rock mass used in the neural implicit learning stage), and $M$ is the number of points in this subset. For each point $p_i \subset P_{sub}$, the spatial coordinates are represented as $X_i = (x_i, y_i, z_i)$, and the corresponding normal vectors are denoted as $n_i = (n_{xi}, n_{yi}, n_{zi})$.

The first stage aims to identify the dominant discontinuities based on orientation similarity. All normal vectors were mapped onto a unit Gaussian sphere. The DBSCAN algorithm was applied in this normal feature space to group points possessing parallel orientations. The Euclidean distance between the unit normal vectors was used as the distance metric.

A point $p_i$ was classified as a core point of a set of discontinuities if there were at least $MinPts_{ori}$ points within its orientation neighbourhood defined by a radius $\epsilon_{\text{ori}}$. Points that do not satisfy the criteria were labelled as noise.

After the first step, points belonging to the same group may represent multiple parallel planes, which are physically disconnected. To further isolate these individual planar surfaces, a secondary spatial segmentation is performed independently within each identified discontinuity. For a specific group of points $P_{sub,k} \subset P_{sub}$ assigned to the $k$-th group, DBSCAN is adopted again, but this time in the 3D Euclidean space without using the normal orientation feature. Two points $p_i, p_j \in P_{sub,k}$ are assigned to the same individual discontinuity according to the same rules defined by the minimum point threshold $MinPts_{spa}$ and the spatial radius $\epsilon_{\text{spa}}$.

Finally, the extracted individual discontinuities are sorted in descending order according to the number of points each contains. The first 5 groups are empirically selected as effective results to avoid the influence caused by point cloud anomalies. The points attributed as noise and those points not belonging to the selected 5 groups are labelled as −1 (negative one).

### 3.3 Validation and comparison

Totally 5 discontinuities were identified through visual inspection and labelled from 1 to 5. $Precision$, $Recall$, and $F1\ score$ are used to comprehensively evaluate the performance of the proposed method, defined as:

$$Precision = (TP/(TP + FP)) \times 100\% \quad (8)$$

$$Recall = (TP/(TP + FN)) \times 100\% \quad (9)$$

$$F1\ score = (2 \times Precision \times Recall)/(Precision + Recall) \times 100\% \quad (10)$$

where:

$TP$ = all correctly predicted points

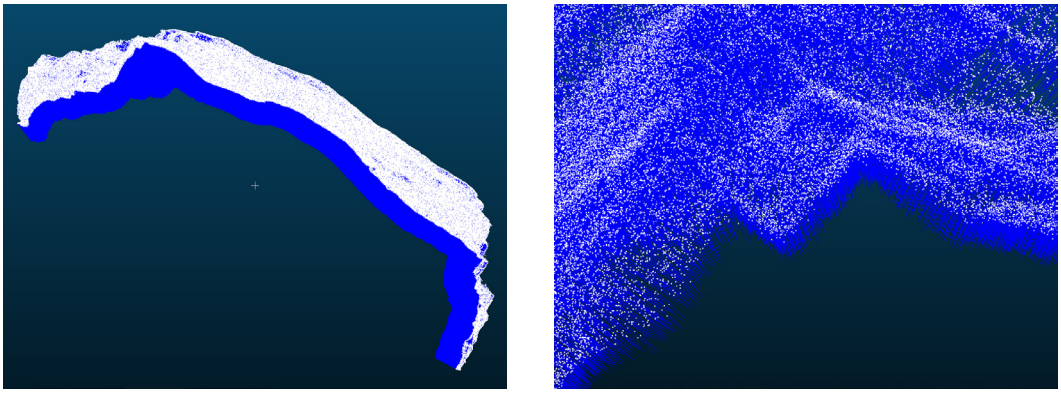
$FP$ = all falsely predicted points

$FN$ = all points not identified.

The method is compared with PCA-based discontinuity identification method. For each point, PCA finds its $k$ nearest neighbours and treats the neighbourhood as an approximation of the underlying surface patch and derives the eigenvalues. The smallest eigenvalue is taken as the normal of the point. However, the accuracy is extremely sensitive to the neighbourhood size and the optimal size is not a pre-known variable. Therefore, in this study, a range of $k$ values were selected for PCA-based method including 10, 15, 20, 30, 50, 80, 120, 200, 300, 500. All other parameters in the clustering process were kept the same for the PCA-based and LGSF-based ManiRock discontinuity identification methods to enable a direct comparison.

## 3.4 Results and discussion

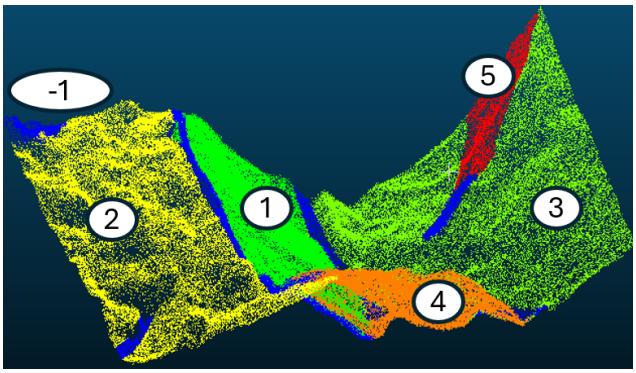
Figure 3a is a manually segmented tunnel surface point cloud to show the derived normals. The points are visualised in white while the normal of each point is visualised in blue. It can be seen the normals are distributed consistently without any flipping, meaning that the normals consistently point to the interior part of the tunnel, which is superior to traditional PCA-based normal estimation method that requires complex post-processing steps to reorient the normals. Figure 3b is an enlarged view of a point with sharp intersections, which shows a clear distinction between surfaces on different structures emphasising the accuracy of the normal estimation from the neural implicit learning method.



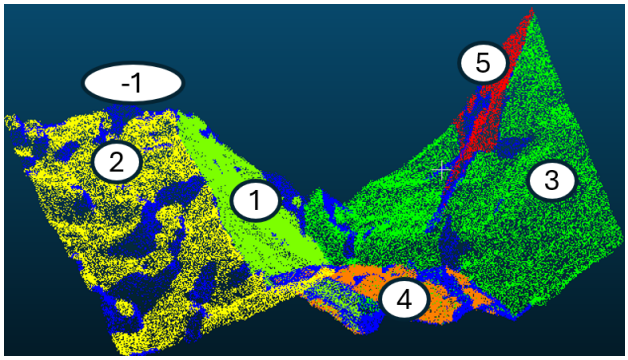
(a) (b)

**Figure 3 Derived normals, white indicates the points, and blue shows the derived normal of each point. (a) A manually segmented tunnel surface. (b) Enlarged view showing the detailed normal orientation**

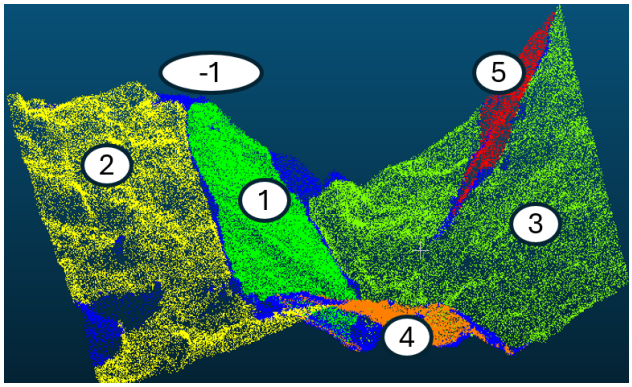
Figure 4a is the manually identified 5 discontinuities of the rock mass point cloud, which serves as the ground truth. The edges and small areas with sharply changed shapes are considered as noise. Figure 4b is the predicted discontinuities by the PCA-based method at its optimal scale. Figure 4c is the predicted discontinuities by ManiRock. It should be noted that points with label −1 visualised in blue contain noise and those points were filtered out in Section 3.2. Points with label −1 are also used in the calculation of the evaluation metrics for scientific rigour.




(a)




(b)




(c)

**Figure 4** **A comparison of the manually identified discontinuities and the predicted discontinuities of the rock mass point cloud. (a) Ground-truth labels. (b) Predicted labels of PCA-based method at its optimal scale. (c) Predicted labels of ManiRock. −1 is used to denote the invalid points visualised in blue. It should be noted that although numbers are ordered according to the number of points in each cluster, due to the 2D visualisation of the 3D point cloud the area of each shape may not reflect the real surface area of each cluster**

Figure 5 shows the results comparison of the ManiRock and multi-scale PCA-based method. ManiRock does not need a preset scale while PCA requires a sensitivity analysis to determine the optimal scale, which is not universal. ManiRock achieved a mean precision of 0.935, a mean recall of 0.875, and a mean F1 score of 0.900. PCA-based method reached its highest performance with $k$ set as 200 and the corresponding mean precision was 0.927, the mean recall was 0.775, and the mean F1 score was 0.839, respectively. ManiRock showed superior performance without relying on the scale selection.

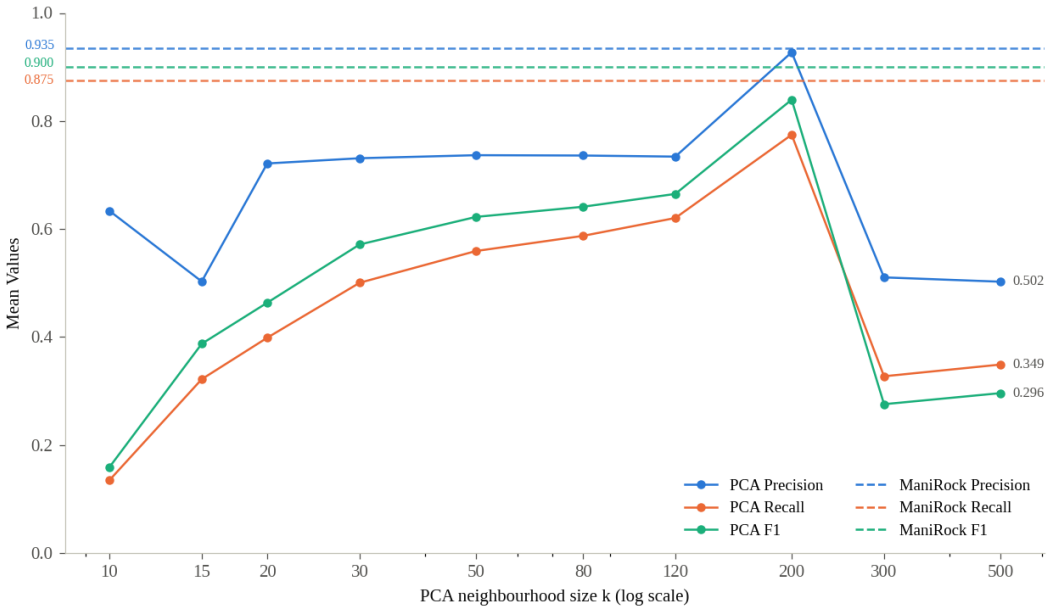



**Figure 5 Comparison of results of ManiRock and multi-scale PCA-based method**

Table 2 lists the detailed results of PCA-based method at different scales and the results of ManiRock method. In the last column, it compared the time cost of normal estimation, which was the only stage in which the 2 pipelines differ since the subsequent two-stage DBSCAN clustering takes 3.2–3.4 s regardless of the normal source. The cost of PCA normals increased with the size $k$. It should be noted that a single PCA run is low cost in time but the appropriate $k$ is unknown a priori and it is dataset dependent. Identifying the optimal scale for PCA method in this study required testing 10 fixed scales (totally 23.2 s) based on ground-truth data reference, which is not available in practice. Although a M3C2-style optimal scale selection strategy (Lague et al. 2013) can be used, the time cost would change dramatically at fine intervals and the mathematical assumptions may not always be met by the point cloud of rough drill-and-blast tunnel surfaces (Han et al. 2026). LGSF used in ManiRock removes the scale parameter and its per-point cost is fixed by the network architecture. In this study it achieved the best results only by running once without using ground-truth labels.

**Table 2 results of precision, recall and F1 score**

| Method | k | Mean precision | Mean recall | Mean F1 | Time* (s) |
|---|---|---|---|---|---|
| Principal component analysis method | 10 | 0.634 | 0.135 | 0.159 | 0.35 |
| | 15 | 0.503 | 0.322 | 0.387 | 0.42 |
| | 20 | 0.721 | 0.399 | 0.463 | 0.50 |
| | 30 | 0.731 | 0.500 | 0.571 | 0.66 |
| | 50 | 0.737 | 0.559 | 0.622 | 0.97 |
| | 80 | 0.736 | 0.587 | 0.641 | 1.46 |
| | 120 | 0.734 | 0.620 | 0.665 | 2.09 |
| | 200 | 0.927 | 0.775 | 0.839 | 3.38 |
| | 300 | 0.510 | 0.327 | 0.275 | 5.02 |
| | 500 | 0.502 | 0.349 | 0.296 | 8.36 |
| ManiRock | – | 0.935 | 0.875 | 0.900 | 155 |

* Time refers normal calculation time only since the subsequent two-stage density-based clustering method segmentation takes 3.2–3.4 s regardless of the normal source.

# 4 Conclusion

This research proposed a hybrid method for accurate and efficient identification of rock mass discontinuities in underground mine tunnels, which integrates unsupervised neural implicit learning and clustering methods. It directly takes the raw point cloud as input and builds a valid manifold for the rock mass surface point cloud and derives a consistent normal field from the trained neural network representing a signed distance function. DBSCAN was then adopted based on the normal orientation feature space and the 3D Euclidean space sequentially to automatically identify the discontinuities of the sample rock mass point cloud. It achieves an average precision of 0.935, a recall of 0.875 and an F1 score of 0.900. This research focused on a geometric proof-of-concept case study from a geometric perspective. However, from a practical ground-support design perspective, the focus was usually on the main structural sets rather than mapping several individual discontinuity patches within such a small area. In the future work, more real-world rock mass point cloud datasets will be used for validating the proposed approach and multi-spectral information including infrared, and R, G, B colours and more spectral bands will be used to distinguish those sharp structures caused by blasts, by forming higher feature dimensions. Although the proposed ManiRock framework is not intended to explicitly design or optimise ground support, it provides an automated first step for extracting the structural geometry required for subsequent geotechnical assessment. Once individual discontinuity surfaces are identified, their orientation, apparent persistence/trace length, spacing and structural-set relationships can be quantified and assessed relative to the excavation geometry. These parameters can then support identification of potentially unstable wedges, slabs or key blocks and evaluation of whether installed reinforcement adequately intersects or constrains the controlling structures. Therefore, it can assist assessment of whether installed bolts adequately intersect the structures controlling potential instability. Future work will provide a more integrated solution.

# References

Assali, P, Grussenmeyer, P, Villemin, T, Pollet, N & Viguier, F 2016, 'Solid images for geostructural mapping and key block modeling of rock discontinuities', *Computers & Geosciences*, vol. 89, pp. 21–31, https://doi.org/10.1016/j.cageo.2016.01.002

Battulwar, R, Emami, E, Zare, M, Battulwar, K, Shahsavar, M, Moniri-Morad, A & Sattarvand, J 2024, 'Utilizing deep learning for the automated extraction of rock mass features from point clouds', *Geotechnical and Geological Engineering*, vol. 42, no. 7, pp. 6179–6194, https://doi.org/10.1007/s10706-024-02886-2

Battulwar, R, Zare-Naghadehi, M, Emami, E & Sattarvand, J 2021, 'A state-of-the-art review of automated extraction of rock mass discontinuity characteristics using three-dimensional surface models', *Journal of Rock Mechanics and Geotechnical Engineering*, vol. 13, no. 4, pp. 920–936, https://doi.org/10.1016/j.jrmge.2021.01.008

Boon, CW, Houlsby, GT & Utili, S 2014, 'Designing tunnel support in jointed rock masses via the DEM', *Rock Mechanics and Rock Engineering*, vol. 48, no. 2, pp. 603–632, https://doi.org/10.1007/s00603-014-0579-8

Chen, J, Fang, Q, Zhang, D & Huang, H 2023, 'A critical review of automated extraction of rock mass parameters using 3D point cloud data', *Intelligent Transportation Infrastructure*, vol. 2, https://doi.org/10.1093/iti/liad005

Chen, J, Yang, T, Zhang, D, Huang, H & Tian, Y 2021, 'Deep learning based classification of rock structure of tunnel face', *Geoscience Frontiers*, vol. 12, no. 1, pp. 395–404, https://doi.org/10.1016/j.gsf.2020.04.003

Erharter, GH, Bar, N, Hansen, TF, Jain, S & Marcher, T 2024, 'International distribution and development of rock mass classification: A review', *Rock Mechanics and Rock Engineering*, vol. 58, no. 10, pp. 11169–11180, https://doi.org/10.1007/s00603-024-04215-8

Ester, M, Kriegel, H-P, Sander, J & Xu, X 1996, 'A density-based algorithm for discovering clusters in large spatial databases with noise', *Proceedings of the Second International Conference on Knowledge Discovery and Data Mining*, AAAI Press, Menlo Park, pp. 226–231.

Fecker, E & Rengers, N 1971, 'Measurement of large scale roughnesses of rock planes by means of profilograph and geological compass', in R Houpert (ed.), *Rock Fracture: Proceedings of the International Symposium on Rock Mechanics*, Ecole Nationale Superieure de Geologie appliquee et de Prospection miniere, Vandœuvre-lès-Nan.

Ferrero, AM, Migliazza, MR & Umili, G 2014, 'Rock mass characterization by means of advanced survey methods', ISRM-EUROCK-2014-002, in *ISRM Regional Symposium – EUROCK 2014*, Vigo.

Ge, Y, Wang, H, Liu, G, Chen, Q & Tang, H 2025, 'Automated identification of rock discontinuities from 3D point clouds using a convolutional neural network', *Rock Mechanics and Rock Engineering*, vol. 58, no. 3, pp. 3683–3700, https://doi.org/10.1007/s00603-024-04351-1

Gigli, G & Casagli, N 2011, 'Semi-automatic extraction of rock mass structural data from high resolution LIDAR point clouds', *International Journal of Rock Mechanics and Mining Sciences*, vol. 48, no. 2, pp. 187–198, https://doi.org/10.1016/j.ijrmms.2010.11.009

Gomes, RK, de Oliveira, LPL, Gonzaga, L, Tognoli, FMW, Veronez, MR & de Souza, MK 2016, 'An algorithm for automatic detection and orientation estimation of planar structures in LiDAR-scanned outcrops', *Computers & Geosciences*, vol. 90, pp. 170–178, https://doi.org/10.1016/j.cageo.2016.02.011

Han, Z, Li, Q, Wang, X & Li, D 2025, 'A physics-guided hierarchical deep learning framework for underground rock reinforcement compliance check based on 4D point cloud data', *Tunnelling and Underground Space Technology*, vol. 164, https://doi.org/10.1016/j.tust.2025.106829

Han, Z, Lin, W, Li, Q & Li, D 2026, 'Full-field deformation quantification of underground tunnels using SLAM LiDAR point cloud based on unsupervised neural implicit learning', *Tunnelling and Underground Space Technology*, vol. 175, https://doi.org/10.1016/j.tust.2026.107777

Kinde, M, Getahun, E & Jothimani, M 2024, 'Geotechnical and slope stability analysis in the landslide-prone area: a case study in Sawla – Laska road sector, Southern Ethiopia', *Scientific African*, vol. 23, https://doi.org/10.1016/j.sciaf.2024.e02071

Lague, D, Brodu, N & Leroux, J 2013, 'Accurate 3D comparison of complex topography with terrestrial laser scanner: application to the Rangitikei canyon (N-Z)', *ISPRS Journal of Photogrammetry and Remote Sensing*, vol. 82, pp. 10–26, https://doi.org/10.1016/j.isprsjprs.2013.04.009

Lato, MJ & Vöge, M 2012, 'Automated mapping of rock discontinuities in 3D lidar and photogrammetry models', *International Journal of Rock Mechanics and Mining Sciences*, vol. 54, pp. 150–158, https://doi.org/10.1016/j.ijrmms.2012.06.003

Li, C, Zhou, J, Du, K & Tao, M 2025a, 'Enhanced discontinuity characterization in hard rock pillars using point cloud completion and DBSCAN clustering', *International Journal of Rock Mechanics and Mining Sciences*, vol. 186, https://doi.org/10.1016/j.ijrmms.2024.106005

Li, K, Zhao, M, Wu, H, Yan, D-M, Shen, Z, Wang, F-Y & Xiong, G 2022, 'GraphFit: Learning multi-scale graph-convolutional representation for point cloud normal estimation', *The Proceedings of the 17th European Conference on Computer Vision,* Springer, Cham, pp. 651–667, https://doi.org/10.1007/978-3-031-19824-3_38

Li, Q, Feng, H, Gong, X & Liu, Y-S 2025b, 'Learning normals of noisy points by local gradient-aware surface filtering', *2025 IEEE/CVF International Conference on Computer Vision (ICCV)*, The Institute of Electrical and Electronics Engineers, Danvers, pp. 28828–28838, https://doi.org/10.1109/ICCV51701.2025.02677

Li, Q, Feng, H, Shi, K, Gao, Y, Fang, Y, Liu, Y-S & Han, Z 2024, 'Learning signed hyper surfaces for oriented point cloud normal estimation', *IEEE Transactions on Pattern Analysis and Machine Intelligence*, vol. 46, no. 12, pp. 9957–9974, https://doi.org/10.1109/tpami.2024.3431221

Li, X, Yao, M, Yuan, J-d, Wang, Y-j & Li, P-y 2023, 'Deep learning characterization of rock conditions based on tunnel boring machine data', *Underground Space*, vol. 12, pp. 89–101, https://doi.org/10.1016/j.undsp.2022.10.010

Maria, FA, Maria, M & Paolo, GG 2004, 'Analysis of tunnel stability: comparison between continuous and discontinuous approaches', *International Journal of Rock Mechanics and Mining Sciences*, vol. 41, pp. 646–651, https://doi.org/10.1016/j.ijrmms.2004.03.113

Milne, D, Hadjigeorgiou, J & Pakalnis, R 1998, 'Rock mass characterization for underground hard rock mines', *Tunnelling and Underground Space Technology*, vol. 13, no. 4, pp. 383–391, https://doi.org/10.1016/S0886-7798(98)00081-9

Palmström, A 1996, 'Characterizing rock masses by the RMi for use in practical rock engineering: Part 1: The development of the Rock Mass index (RMi)', *Tunnelling and Underground Space Technology*, vol. 11, no. 2, pp. 175–188.

Priest, SD 1993, *Discontinuity analysis for rock engineering*, Springer, Dordrecht.

Pu, C, Zhan, J, Huang, D, Zhu, W & Peng, J 2025, 'Interpretation and characterization of sedimentary rock mass structure using UAV multi-sensor data', *Rock Mechanics and Rock Engineering*, vol. 58, no. 7, pp. 8415–8443, https://doi.org/10.1007/s00603-025-04514-8

Singh, SK, Raval, S & Banerjee, BP 2021, 'Automated structural discontinuity mapping in a rock face occluded by vegetation using mobile laser scanning', *Engineering Geology*, vol. 285, https://doi.org/10.1016/j.enggeo.2021.106040

Tang, N, Wang, L, Jiang, H, Huang, X, Tan, G & Zhou, X 2023, 'A new clustering method of rock discontinuity sets based on modified K-means algorithm', *Bulletin of Engineering Geology and the Environment*, vol. 82, no. 11, pp. 415, https://doi.org/10.1007/s10064-023-03406-x

Wang, R, Zhan, J, An, X, Yao, Z & Peng, J 2026, 'Efficient method for identification of rock mass discontinuities using 3D point cloud data', *Rock Mechanics and Rock Engineering*, in press, https://doi.org/10.1007/s00603-026-05603-y

Xu, H & Tang, S 2025, 'Digital tunnel geometry model (DTGM): A multimodal data fusion framework for rock mass feature quantification', *International Journal of Rock Mechanics and Mining Sciences*, vol. 194, https://doi.org/10.1016/j.ijrmms.2025.106212

Yi, X, Feng, W, Wang, D, Yang, R, Hu, Y & Zhou, Y 2023, 'An efficient method for extracting and clustering rock mass discontinuities from 3D point clouds', *Acta Geotechnica*, vol. 18, no. 7, pp. 3485–3503, https://doi.org/10.1007/s11440-023-01803-w

Zhan, J, Chen, J, Xu, P, Zhang, W, Han, X & Zhou, X 2017a, 'Automatic identification of rock fracture sets using finite mixture models', *Mathematical Geosciences*, vol. 49, no. 8, pp. 1021–1056, https://doi.org/10.1007/s11004-017-9702-1

Zhan, J, Xu, P, Chen, J, Wang, Q, Zhang, W & Han, X 2017b, 'Comprehensive characterization and clustering of orientation data: A case study from the Songta dam site, China', *Engineering Geology*, vol. 225, pp. 3–18, https://doi.org/10.1016/j.enggeo.2017.01.010

Zhou, J-w, Chen, J-l & Li, H-b 2024, 'An optimized fuzzy K-means clustering method for automated rock discontinuities extraction from point clouds', *International Journal of Rock Mechanics and Mining Sciences*, vol. 173, https://doi.org/10.1016/j.ijrmms.2023.105627

Zhou, Z, Yu, J, Gao, J, Cai, X & Wang, Z 2025, 'Rapid rock mass classification framework using machine learning and semantic segmentation for underground mining', *Engineering Applications of Artificial Intelligence*, vol. 159, https://doi.org/10.1016/j.engappai.2025.111530